

Predicting Wettability and the Electrochemical Window of Lithium-Metal/Solid Electrolyte Interfaces

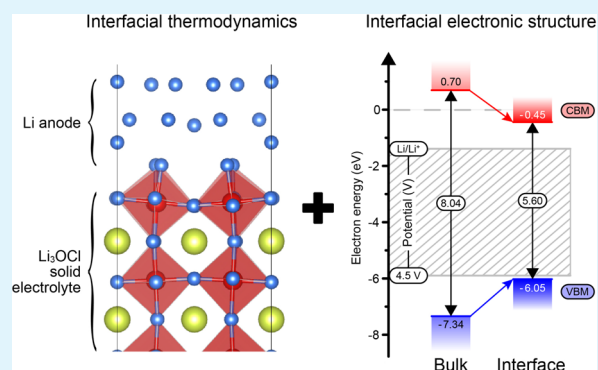
Kwangnam Kim[†] and Donald J. Siegel^{*,†,‡,§,||,⊥}

[†]Mechanical Engineering Department, [‡]Materials Science & Engineering, [§]Applied Physics Program, ^{||}University of Michigan Energy Institute, and [⊥]Joint Center for Energy Storage Research, University of Michigan, Ann Arbor, Michigan 48109-2125, United States

Supporting Information

ABSTRACT: The development of solid electrolytes (SEs) is expected to enhance the safety of lithium-ion batteries. Additionally, a viable SE could allow the use of a Li-metal negative electrode, which would increase energy density. Recently, several antiperovskites have been reported to exhibit high ionic conductivities, prompting investigations of their use as an SE. In addition to having a suitable conductivity, phenomena at the interface between an SE and an electrode are also of great importance in determining the viability of an SE. For example, interfacial interactions can change the positions of the band edges of the SE, altering its stability against undesirable oxidation or reduction. Furthermore, the wettability of the SE by the metallic anode is desired to enable low interfacial resistance and uniform metal plating and stripping during cycling. The present study probes several properties of the SE/electrode interface at the atomic scale. Adopting the antiperovskite SE Li_3OCl (LOC)/Li-metal anode interface as a model system, the interfacial energy, work of adhesion, wettability, band edge shifts, and the electrochemical window are predicted computationally. The oxygen-terminated interface was determined to be the most thermodynamically stable. Moreover, the large calculated work of adhesion for this system implies that Li will wet LOC, suggesting the possibility for low interfacial resistance. Nevertheless, these strong interfacial interactions come at a cost to electrochemical stability: strong interfacial bonding lowers the energy of the conduction band minimum (CBM) significantly and narrows the local band gap by 30% in the vicinity of the interface. Despite this interface-induced reduction in electrochemical window, the CBM in LOC remains more negative than the Li/Li^+ redox potential, implying stability against reduction by the anode. In sum, this study illustrates a comprehensive computational approach to assessing electrode/electrolyte interfacial properties in solid-state batteries.

KEYWORDS: battery, energy storage, interface, Li-metal anode, wettability, electrochemical window



INTRODUCTION

Lithium-ion batteries (LIBs) are widely used energy storage devices due to their relatively high energy density and rechargeability.¹ Commercial LIBs typically employ liquid electrolytes, which have the advantage of high ionic conductivities. However, commonly used liquid electrolytes are flammable, volatile, and susceptible to Li dendrite formation, resulting in internal short-circuiting.^{1–3} Thus, improvements in cell designs and/or materials that address these safety concerns are desirable. Compared to liquids, solid electrolytes (SEs) are less flammable, nonvolatile, and less sensitive to changes in temperature.^{1,4–6} Also, the high stiffness exhibited by some SEs has been projected to suppress dendrite formation.⁷ This latter benefit presents the possibility to increase the capacity of the negative electrode by substituting metallic lithium for lithiated carbon.⁸

Low ionic conductivity has historically been a shortcoming of SE.⁵ More recently, however, a growing number of solid ionic conductors have been reported with conductivities comparable to those of liquids.^{9–15} Nevertheless, subsequent

investigations on these SEs have shown that a high ionic conductivity alone is insufficient for realizing a viable solid-state cell; interfacial interactions involving the electrodes are also critical.¹⁵ Two examples of important interfacial properties involving SE are stability^{1,16–19} and wettability.^{20–22}

Insufficient interfacial stability manifests through the formation of new phases (from reactions between the SE and electrode, or through decomposition of the SE itself) or through electron transfer between the electrode and SE. Both processes can yield undesirable outcomes. In the former case, the product phases can limit Li-ion mobility and thus increase interfacial resistance.^{16,18} In the latter mechanism, electron transfer to/from the SE can precipitate additional chemical reactions or impart undesirable electrical conductivity to the SE: for example, the reduction of an SE by the negative electrode can inject electrons into the conduction band.^{23,24}

Received: July 27, 2019

Accepted: October 2, 2019

Published: October 2, 2019

Figure 1 presents an energy level diagram for an SE and the electrodes in a battery.^{1,23} To minimize electron transfer to/

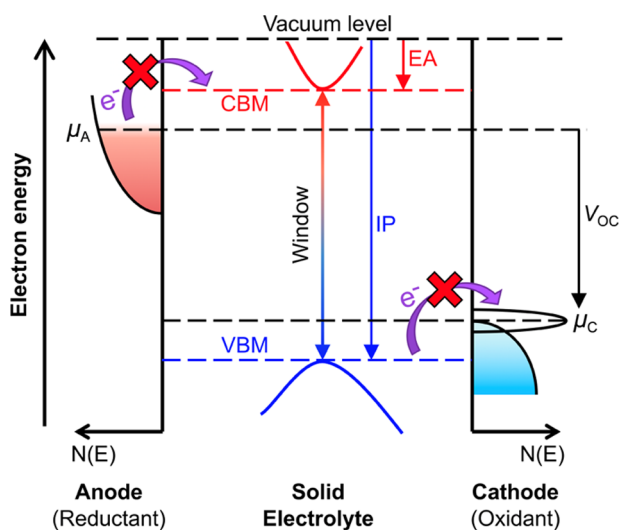


Figure 1. Energy levels of a solid electrolyte (SE) with respect to the density of states, $N(E)$, of the electrodes. Red and blue bands represent the conduction and valence bands of the SE, respectively. The electrolyte is susceptible to reduction by the anode when the electrochemical potential of the anode, μ_A , is located at higher energy than the conduction band minimum, CBM, of the SE. Similarly, the oxidation of the SE can occur when the energy of the valence band maximum, VBM, is higher than the electrochemical potential of the cathode, μ_C . The open-circuit voltage (V_{OC}), ionization potential (IP), and electron affinity (EA) are also shown.

from an SE, the anode electrochemical potential, μ_A , should be located below (i.e., at a lower energy than) the conduction band minimum (CBM) of the SE, while the electrochemical potential of the cathode, μ_C , should be at a higher energy than the SE's valence band maximum (VBM). Prior studies have demonstrated that these levels can be predicted computationally for an interface-free (i.e., bulk) SE, providing an estimate of an SE's susceptibility to undesirable electron transfer.^{24–26} Nevertheless, the electrochemical window of an electrolyte can be influenced by interfacial interactions with the electrodes. For example, a previous report revealed that the highest unoccupied molecular orbital/lowest unoccupied molecular orbital levels of electrolyte solvent molecules shift due to interactions with electrode surfaces, narrowing the electrochemical window relative to that of the isolated molecules.²³ To the best of our knowledge, the impact of interface interactions on the CBM/VBM positions of an SE has not been reported.

Regarding interfacial bonding, recent studies have identified the wettability of an SE by Li metal as a key factor in predicting performance.^{27,28} Low wettability results in poor contact between Li and an SE, resulting in current focusing, high interfacial resistance, and/or dendrite formation.^{20,21,29–31} For $\text{Li}_7\text{La}_3\text{Zr}_2\text{O}_{12}$, improved wetting by Li can be achieved through interface coatings^{20,29,32,33} or surface cleaning treatments.^{22,30} Despite the importance of wettability to SE performance, few computational studies of wettability have been reported.²²

The present study predicts stability and wettability at a Li-metal/SE interface. The antiperovskite with composition Li_3OCl (LOC) is adopted as a model SE.¹² LOC is one example of several antiperovskite compositions that have been

reported as potential SEs; others include Li_3OBr , Na_3OCl , Na_3OBr , and Na_3OI .^{12,34,35} LOC has a simple crystal structure, making it attractive for computationally expensive electronic structure calculations. Furthermore, LOC has been reported to have a high ionic conductivity ($\sim 10^3$ S/cm) and a large band gap,^{26,36} the latter implying a wide electrochemical window. An LOC-based cell with a graphitic anode and LiCoO_2 -based cathode was reported to operate at a voltage of up to 4.2 V over many cycles,³⁷ additional experiments using a Li–LOC–Li symmetric cell reported that LOC is compatible with a Li-metal anode.^{37,38}

First-principles calculations were used to assess the electronic and thermodynamic properties of Li and LOC surfaces/interfaces. Vibrational contributions to the enthalpy and entropy were evaluated to estimate surface/wettability energies at near-ambient temperatures. Interface wettability was characterized according to the Li contact angle on LOC, derived from the Young–Dupré equation and the calculated interfacial work of adhesion. Stability against reduction by the Li electrode was predicted by determining the absolute positions of the band edges of LOC (via GW calculations) in relation to the Li/ Li^+ level.

These calculations suggest that the oxygen-terminated Li/LOC interface is the most thermodynamically stable. The calculated work of adhesion implies that Li will wet LOC with a low contact angle, suggesting the possibility for strong interfacial bonding and low interfacial resistance. On the other hand, this strong interfacial interaction significantly narrows the band gap of LOC in the interfacial region by shifting both the CBM and VBM: in the vicinity of the interface, the bulk band gap of ~ 8 eV is reduced to ~ 5.6 eV, implying a trade-off between strong interfacial bonding/wettability and electrochemical stability. Despite this interface-induced reduction in electrochemical window, the CBM in LOC remains ~ 1 V more negative than the Li/ Li^+ redox potential, denoting stability against reduction by the anode. In total, the present study demonstrates how first-principles computational methods can be used to comprehensively characterize interfacial properties that are relevant to the operation of solid-state batteries.

METHODS

First-Principles Calculations. Density functional theory (DFT) calculations were performed using the Vienna ab initio Simulation Package.³⁹ Exchange–correlation effects were treated within the generalized gradient approximation (GGA), as parameterized by Perdew, Burke, and Ernzerhof (PBE).⁴⁰ Interactions between core and valence electrons were treated using the projector augmented wave method.^{41,42} The valence electron configurations were $1s^2 2s$ for Li, $2s^2 2p^4$ for O, and $3s^2 3p^5$ for Cl. A plane-wave basis set with a cutoff energy of 550 eV was used for calculations involving ionic relaxations and total energy evaluations. More computationally expensive GW calculations (described below) used a 2s valence configuration for Li and lower cutoff energy of 475 eV. The energy of the electronic ground state was converged to within 10^{-5} eV, and the force criterion for atomic relaxations was set to 0.01 eV/Å. Convergence tests with respect to k -point sampling density for bulk systems are discussed in the Supporting Information.

Surface energies for LOC were calculated for fully relaxed slab models with 11 layers and within a supercell containing a 12 Å vacuum region. A Γ -centered $4 \times 4 \times 1$ k -point mesh was used for all surface calculations. The effects of the number of slab layers (7–15 layers) and vacuum thicknesses (6–24 Å) were tested; it was determined that the surface energy was well converged using the parameters described above. The work of adhesion was calculated for

fully relaxed interface models with seven layers of LOC and seven layers of Li. Convergence testing revealed that the work of adhesion did not change significantly upon increasing the number of Li and LOC layers (tests were done with 5–13 Li layers and 7–23 LOC layers). A Γ -centered $4 \times 4 \times 1$ k -point mesh was also used for interface calculations; this sampling converged the total energy of the interface to within 1 meV/atom. Spin-polarized calculations were used for gas-phase molecules and for atoms; these systems used a simulation cell of dimensions $10 \text{ \AA} \times 11 \text{ \AA} \times 12 \text{ \AA}$, with reciprocal space sampled at the Γ point.

Free energies were evaluated within the harmonic approximation using the direct method.⁴³ Atomic displacements of ± 0.02 and ± 0.04 \AA were used in conjunction with $3 \times 3 \times 3$ expansions of the conventional unit cells, corresponding to supercells containing 135 atoms for LOC (Figure S1), 54 atoms for BCC Li, 324 atoms for Li_2O , and 216 atoms for LiCl. A Γ -centered $4 \times 4 \times 4$ k -point mesh was used for the Li supercell, whereas a single k -point was used for the other systems. Phonon calculations on slab models of LOC (see Figure S2) employed a 3×3 expansion within the surface plane for (100) surfaces, a 3×2 expansion for (110) surfaces, and a 2×1 expansion for (111) surfaces. A single k -point was used for these slab models. Interface models used a 2×2 expansion within the interfacial plane (dimensions of $15.6 \text{ \AA} \times 15.6 \text{ \AA}$) and a Γ -centered $2 \times 2 \times 1$ k -point mesh. Convergence testing revealed that increases to system size or the number of k -points did not significantly alter the vibrational properties.

Band edge positions for the conduction and valence bands were calculated with the GW method.^{44,45} Prior studies have shown that GW calculations yield ionization potentials (IPs), electron affinities (EAs), and band gaps in good agreement with (inverse) photoemission experiments.^{46–50} We performed non-self-consistent G_0W_0 and (partially) self-consistent GW_0 and GW calculations using input wave functions from either self-consistent GGA or HSE06^{51,52} hybrid-functional calculations. Here, “G” and “W” refer to Green’s function and the screened Coulomb interaction, respectively. In the self-consistent GW methods, the eigenvalues are updated, while the wave functions are kept fixed.

Band Edge Positions. The absolute positions of the VBM and CBM (relative to vacuum) in bulk LOC were obtained following the procedure described in ref 53. Figure 2 summarizes this approach, which involves aligning the planar-averaged electrostatic potential (V_{ref}) in the bulk region of an LOC surface slab with that from a bulk cell.^{24,49,50} VBM and CBM positions in the bulk cell (given by ϵ_{VBM} and ϵ_{CBM}) are evaluated using GW calculations, while the position of the vacuum level (V_{vac}) is determined from the slab system at a lower level of theory (GGA or HSE06). Aligning the electrostatic potentials

in these two systems provides a common reference from which the absolute VBM/CBM positions can be inferred. Following this procedure, the IP of bulk LOC is expressed as

$$\text{IP}^{\text{b,GW}} = (V_{\text{vac}}^{\text{s}} - V_{\text{ref}}^{\text{s}}) - (\epsilon_{\text{VBM}}^{\text{b,GW}} - V_{\text{ref}}^{\text{b,GW}})$$

where $V_{\text{vac}}^{\text{s}}$ and $V_{\text{ref}}^{\text{s}}$ are the planar-averaged electrostatic potentials in the vacuum region and at the center of the LOC slab, respectively, and $\epsilon_{\text{VBM}}^{\text{b,GW}}$ and $V_{\text{ref}}^{\text{b,GW}}$ are the VBM energy and reference electrostatic potential of bulk LOC evaluated with the GW method, respectively. $V_{\text{ref}}^{\text{b,GW}}$ for the bulk cell should be evaluated at an atomic plane similar to that found in the center of the LOC slab. The absolute CBM position (i.e., $\text{EA}^{\text{b,GW}}$) can be determined by combining $\text{IP}^{\text{b,GW}}$ with the bulk band gap (i.e., $E_{\text{g}}^{\text{b,GW}}$). Since the wave functions input to a GW calculation (from a preceding GGA or HSE06 calculation) are unchanged during the GW calculation, the Hartree potential is also unchanged. Thus, the reference potential from the slab supercell (evaluated using the GGA or HSE06 functional) and the bulk (evaluated using GW) can be aligned without difficulty.^{49,50}

In a similar fashion, the absolute positions of the LOC band edges can be determined when LOC is interfaced with a Li anode. In this case, the electrostatic potential at the center of an LOC slab (now a subcomponent of the interface supercell) is used as the reference potential (i.e., $V_{\text{ref}}^{\text{i,GW}}$). Band edge shifts are obtained as the difference in VBM or CBM positions between the bulk and interface systems as

$$\Delta\epsilon_{\text{VBM/CBM}}^{\text{b-i,GW}} = |\epsilon_{\text{VBM/CBM}}^{\text{i,GW}} - \epsilon_{\text{VBM/CBM}}^{\text{b,GW}}|$$

Gibbs Free-Energy Calculations. The Gibbs free energy, G , for several phases relevant for the Li–O–Cl system was evaluated using the following expression^{54–56}

$$G(T, P) = E(0 \text{ K}) + E^{\text{vib}}(T) + E^{\text{rot}}(T) + E^{\text{trans}}(T) + pV - T[S^{\text{vib}}(T) + S^{\text{conf}}(T)]$$

Here $E(0 \text{ K})$ is the static energy at 0 K (i.e., the DFT total energy), and $E^{\text{vib}}(T)$ is the vibrational energy, including the zero-point energy. For molecular systems, the rotational energy, $E^{\text{rot}}(T)$, translational energy, $E^{\text{trans}}(T)$, and the pV term sum to $7/2k_{\text{B}}T$ ($4k_{\text{B}}T$) for linear (nonlinear) molecules, where k_{B} is the Boltzmann constant. These three terms do not significantly contribute to the free energy of solids under the conditions examined here. $S^{\text{vib}}(T)$ and $S^{\text{conf}}(T)$ are the vibrational and configurational entropies; the latter term can be neglected for the ordered solid systems examined here.^{56,57} For gas-phase molecules, the total entropy $S^{\text{vib}}(T) + S^{\text{conf}}(T)$ was obtained from experimental data.⁵⁸ Vibrational contributions to the energy and entropy within the harmonic approximation can be expressed as⁵⁴

$$E^{\text{vib}}(T) = \sum_i \frac{1}{2} \hbar \omega_i + \hbar \omega_i (e^{\hbar \omega_i / k_{\text{B}} T} - 1)^{-1}$$

$$S^{\text{vib}}(T) = k_{\text{B}} \sum_i \frac{\hbar \omega_i / k_{\text{B}} T}{e^{\hbar \omega_i / k_{\text{B}} T} - 1} - \ln(1 - e^{-\hbar \omega_i / k_{\text{B}} T})$$

where the sums are over vibrational modes ω_i , and \hbar is the reduced Planck constant.

The dependence of the chemical potentials of the gas-phase species upon temperature and pressure was evaluated assuming ideal gas behavior

$$\mu(T, p) = \frac{1}{2} \left[G(T, p^\circ) + k_{\text{B}} T \ln \left(\frac{p}{p^\circ} \right) \right]$$

where p° is the standard pressure. The calculated vibrational modes for the various molecular species, 1572 cm^{-1} for O_2 , 538 cm^{-1} for Cl_2 , 1062 , 916 , and 424 cm^{-1} for ClO_2 , and 642 , 577 , and 278 cm^{-1} for Cl_2O , are in reasonable agreement with the experimental data.⁵⁸ A discussion of corrections to the chemical potentials of oxygen and chlorine can be found in the Supporting Information.

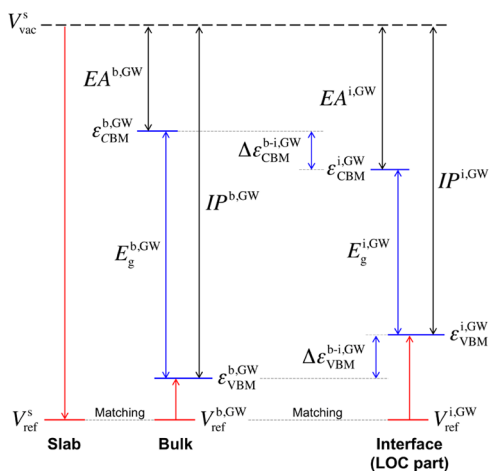


Figure 2. Determination of the absolute band edge positions of a solid electrolyte. The method is based on aligning the reference potentials V_{ref} of the slab (s), bulk (b), and interface (i) systems.

RESULTS AND DISCUSSION

Bulk Properties. Antiperovskite LOC crystallizes in the cubic space group $Pm\bar{3}m$. In this structure, Li_6O octahedra are surrounded by a cubic framework composed of Cl anions (Figure S1).¹² The low-energy structures of LOC, BCC Li, Li_2O , and LiCl were determined at 0 K using the Murnaghan equation of state (see the section Murnaghan equation of state and Figure S3 in the Supporting Information).⁵⁹

Table 1 summarizes the band-gap predictions as a function of the calculation method and input wave-function flavor

Table 1. Calculated Band Gaps (in Electron Volts) for Li_3OCl as a Function of the Calculation Method^a

wave-function type	non-GW	G_0W_0	GW_0	GW
GGA-PBE	4.84	7.29	7.84	8.65
HSE06	6.41	8.04	8.32	8.80

^aTwo different exchange–correlation functionals, GGA-PBE and HSE06, were used to generate the input wave functions used in the GW calculations.

(based on either a self-consistent GGA or hybrid-functional calculation). GW calculations were preceded by extensive convergence tests, as described in the section GW calculations and Figures S4 and S5 in the Supporting Information. Of the GW methods reported in Table 1, prior studies have shown that the HSE06 + G_0W_0 method and the GGA + GW_0 method yield band gaps that are in very good agreement with experiments.^{46,47,60} In the case of LOC, these two methods suggest that the band gap lies within the range 7.8–8.1 eV. This large band gap compares favorably with those reported for other solid electrolytes, which are typically smaller: for example, 6.4 eV for $\text{Li}_7\text{La}_3\text{Zr}_2\text{O}_{12}$ (HSE06 + G_0W_0),²⁴ 2.1 eV for $\text{Li}_6\text{PS}_3\text{Br}$ (GGA),⁶¹ and 3.7 eV for $\text{Li}_{10}\text{GeP}_2\text{S}_{12}$ (HSE).²⁵

Bulk Stability. Figure 3a illustrates the stability range for bulk LOC at 300 K as a function of the chemical potentials for oxygen, $\mu_{\text{O}}^{\text{LOC}}$, and chlorine, $\mu_{\text{Cl}}^{\text{LOC}}$, in LOC. This stability plot was generated by expressing the Gibbs free energy of LOC in terms of the chemical potentials of its constituents, as

$$G_{\text{Li}_3\text{OCl}}^{\text{bulk}} = 3\mu_{\text{Li}}^{\text{LOC}} + \mu_{\text{O}}^{\text{LOC}} + \mu_{\text{Cl}}^{\text{LOC}} \quad (1)$$

To avoid decomposition of LOC into the elements or binary compounds, the range of allowable values for its chemical potentials must satisfy the following constraints⁶²

$$\begin{aligned} \mu_{\text{Li}}^{\text{LOC}} &\leq G_{\text{Li}}^{\text{BCC bulk}} = \mu_{\text{Li}}^{\text{ref}} \\ \mu_{\text{O}}^{\text{LOC}} &\leq 0.5G_{\text{O}_2}^{\text{gas}} = \mu_{\text{O}}^{\text{ref}} \\ \mu_{\text{Cl}}^{\text{LOC}} &\leq 0.5G_{\text{Cl}_2}^{\text{gas}} = \mu_{\text{Cl}}^{\text{ref}} \\ 2\mu_{\text{Li}}^{\text{LOC}} + \mu_{\text{O}}^{\text{LOC}} &\leq G_{\text{Li}_2\text{O}}^{\text{bulk}} \\ \mu_{\text{Li}}^{\text{LOC}} + \mu_{\text{Cl}}^{\text{LOC}} &\leq G_{\text{LiCl}}^{\text{bulk}} \\ x\mu_{\text{Cl}}^{\text{LOC}} + y\mu_{\text{O}}^{\text{LOC}} &\leq G_{\text{Cl}_x\text{O}_y}^{\text{gas}} \end{aligned} \quad (2)$$

where the superscript “ref” refers to standard conditions, and Cl_xO_y refers to Cl_2O and ClO_2 gases at STP.⁵⁸ $\mu_{\text{Li}}^{\text{LOC}}$ can be eliminated in eq 2 using eq 1, allowing the constraints to be expressed only as functions of $\mu_{\text{O}}^{\text{LOC}}$ and $\mu_{\text{Cl}}^{\text{LOC}}$.

The narrow blue region in Figure 3a identifies the range of chemical potentials (satisfying the above constraints) for which LOC is stable at 300 K and 1 atm. Four constraints define the region’s boundaries: at the left and right edges, two parallel lines demark decomposition into Li_2O and LiCl , while boundaries above and below mark the chemical potentials at which decomposition into O_2 gas or to Li metal is expected. Red lines and arrows in Figure 3a indicate the chemical potential values at which other decomposition products are predicted to form. Although not shown, the stability range for LOC at 550 K and 10^{-8} atm, conditions typical for its synthesis,¹² is very similar to that shown in Figure 3a at 300 K and 1 atm.

The combination of chemical potential values (parallel lines in Figure 3a) that bound the stability regime of LOC can be expressed generally as $\mu_{\text{O}}^{\text{LOC}} - 2\mu_{\text{Cl}}^{\text{LOC}} = C$, where C is a constant. At 300 K and 1 atm, LOC is stable for $1.39 \leq \mu_{\text{O}}^{\text{LOC}} - 2\mu_{\text{Cl}}^{\text{LOC}} \leq 1.42$. Since the stability region is very narrow, $\mu_{\text{O}}^{\text{LOC}}$ and $\mu_{\text{Cl}}^{\text{LOC}}$ can be related by assuming $C = 1.4$, e.g., $\mu_{\text{Cl}}^{\text{LOC}} = 0.5(\mu_{\text{O}}^{\text{LOC}} - 1.4)$. With this approximation, the constraints in eq 2 can be expressed only in terms of $\mu_{\text{O}}^{\text{LOC}}$.

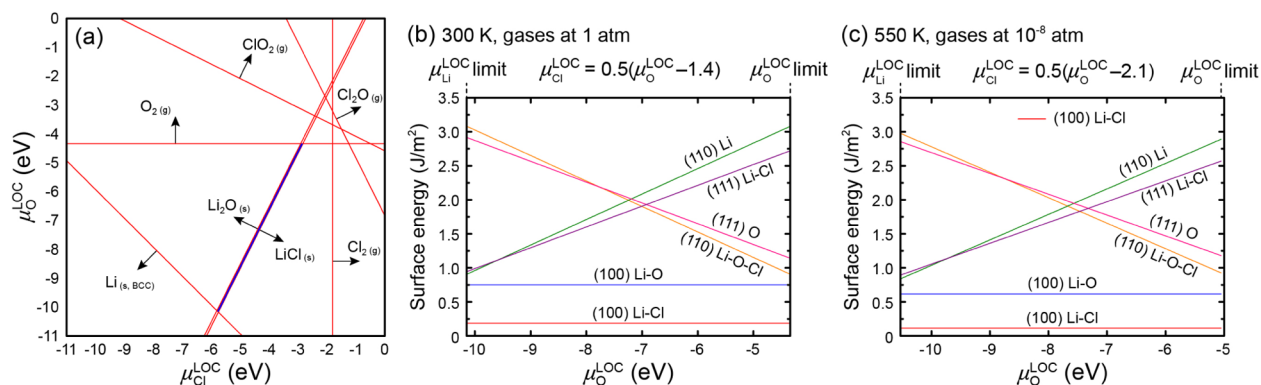


Figure 3. (a) Stability of bulk LOC at 300 K and 1 atm as a function of the chemical potentials of oxygen ($\mu_{\text{O}}^{\text{LOC}}$) and chlorine ($\mu_{\text{Cl}}^{\text{LOC}}$) in LOC. The thin blue region indicates the combination of chemical potentials that satisfy the thermodynamic constraints in eq 2, resulting in the stability of LOC. Outside of this region, LOC is expected to decompose into other phases; red lines and arrows indicate boundaries in chemical potential space where other phases are predicted to form. (b, c) Calculated surface energies of LOC as a function of the chemical potential of oxygen at 300 K and 1 atm [panel (b), STP] and at 550 K and 10^{-8} atm [panel (c), comparable to the synthesis conditions of LOC]. In the surface energy plots, the chemical potentials $\mu_{\text{Cl}}^{\text{LOC}}$ and $\mu_{\text{O}}^{\text{LOC}}$ are related by eq 2 and restricted to the range determined in panel (a) for which LOC is stable with respect to decomposition.

Li₃OCl Surface Energies. The stability of six low-index surfaces of LOC was examined (Figure S2): two (100) surfaces, one with Li–Cl termination and one with Li–O termination; two (110) surfaces, one terminated by Li and one terminated by a plane containing all of Li, O, and Cl; and two (111) surfaces, one with Li–Cl termination and one O termination. To ensure both surfaces of each LOC slab were identical, it was necessary to construct nonstoichiometric slabs. The surface energy was evaluated as

$$\sigma = \frac{1}{A} (G_{\text{slab}} - \sum_i n_i^{\text{slab}} \mu_i^{\text{LOC}})$$

where A is the surface area, G_{slab} is the Gibbs free energy of the slab supercell, n_i^{slab} is the number of atoms of type i in the slab, and μ_i^{LOC} is the chemical potential of species i in bulk LOC. The chemical potential of Li ($\mu_{\text{Li}}^{\text{LOC}}$) in the above expression for σ can be eliminated using the Gibbs free energy of LOC (eq 1); furthermore, the chemical potential of Cl ($\mu_{\text{Cl}}^{\text{LOC}}$) can also be eliminated using the relation $\mu_{\text{Cl}}^{\text{LOC}} = 0.5(\mu_{\text{O}}^{\text{LOC}} - C)$ so that the surface energy can be expressed as a function of $\mu_{\text{O}}^{\text{LOC}}$

$$\sigma = \frac{1}{A} \left\{ G_{\text{slab}} - \left[\frac{1}{3} n_{\text{Li}}^{\text{slab}} G_{\text{Li}_3\text{OCl}}^{\text{bulk}} - \frac{1}{2} \left(n_{\text{Cl}}^{\text{slab}} - \frac{1}{3} n_{\text{Li}}^{\text{slab}} \right) C + \left(n_{\text{O}}^{\text{slab}} + \frac{1}{2} n_{\text{Cl}}^{\text{slab}} - \frac{1}{2} n_{\text{Li}}^{\text{slab}} \right) \mu_{\text{O}}^{\text{LOC}} \right] \right\}$$

where $C = 1.4$ at 300 K and 1 atm.

Figures 3b,c compare the energies of the six examined surfaces of LOC as a function of oxygen chemical potential at STP (Figure 3b) and at conditions typical of LOC synthesis (550 K, low pressure, Figure 3c). Compared to the (111) and (110) surfaces, the (100) planes have the lowest surface energies regardless of their chemical termination. Calculated surface energies for the (100) surfaces are 0.19 and 0.75 J/m² at 300 K and 0.11 and 0.62 J/m² at 500 K, for the Li–Cl and Li–O terminations, respectively. Assuming that thermodynamic equilibrium holds, this implies that the (100) surfaces are the most plausible; indeed, the equilibrium crystallite shapes predicted by the Wulff construction and the calculated surface energies exhibit only (100) planes, Figure S6.⁶³ Given their low energies, the (100) surfaces were adopted for additional interfacial analyses, as described below. Note that the surface energies of (100) planes are independent of $\mu_{\text{O}}^{\text{LOC}}$, as explained in the Supporting Information.

Li/Li₃OCl Interface. LOC/Li interfaces were constructed by joining either Li–Cl-terminated (100) or Li–O-terminated (100) surfaces of LOC with the (100) surface of a Li metal. The minimum-energy interface geometry was determined by searching over a series of rigid displacements of the adjoining slabs in directions within, and normal to, the interface plane. The equilibrium interfacial distance (assuming rigid slabs) was determined by fitting energy vs interface distance data to the universal binding energy relation (UBER).⁶⁶ Starting from this interface distance, all atoms were subsequently fully relaxed to generate the final interface geometry.

Hereafter, we refer to the (100) LOC surface or interface with either Li–Cl or Li–O termination as the “Cl-terminated” or “O-terminated” surface, respectively. Interfaces involving each of these two LOC surfaces and the (100) surface of BCC Li were modeled to predict the interfacial thermodynamics, wettability, and electrochemical stability of LOC in contact with a Li-metal anode. The (100) surface of Li has the lowest

energy among low-index facets of BCC Li: 29.1, 30.5, and 31.2 meV/Å² for (100), (110), and (111) planes, respectively, Figure S7, similar to previous reports.^{65–67} Interfaces were constructed by matching the 2 × 2 Cl- or O-terminated LOC (100) surface to a $\sqrt{5} \times \sqrt{5}$ (100) BCC Li surface containing five Li atoms per layer. This interfacial orientation relationship minimizes the interfacial strain while allowing for moderate supercell sizes. The Li surface was strained by 1.1% in its in-plane directions to match the dimensions of the LOC slab. The interface models contained 103 and 107 atoms, respectively, for supercells based on Cl- and O-terminated LOC.

To identify the minimum-energy interface geometry, the total energy of the interface was evaluated as a function of displacements within, and normal to, the interface plane. One hundred interfacial displacements in the interfacial plane were sampled using a uniform grid with a 10 × 10 mesh. This grid search was performed at several interlayer distances. In all cases, the atom positions were fixed. The interfacial work of adhesion W_{ad} at each interfacial separation, d , was calculated for this “rigid” interface according to

$$W_{\text{ad}}(d) = \frac{1}{A} [E_{\text{interface}}(d) - (E_{\text{Li}_3\text{OCl}} + E_{\text{BCC-Li}})]$$

where A is the interface area and $E_{\text{interface}}$, E_{LOC} , and $E_{\text{BCC-Li}}$ are the total energies of the interface, the isolated LOC slab, and the isolated BCC Li slab, respectively. (The dimensions and the number of layers contained in the isolated slabs were identical to those in the interface system.) The W_{ad} values obtained at different interfacial separations were fit using the universal binding energy relation (UBER)⁶⁴

$$W_{\text{ad}}(d) = -W_{\text{ad}}^0 \left(1 + \frac{d - d_0}{l} \right) e^{-(d-d_0)/l}$$

where W_{ad}^0 is the work of adhesion for the rigid interface at the equilibrium separation, d_0 , and l is a scaling length. The equilibrium separations for the Cl- and O-terminated interfaces were 3.11 and 2.61 Å, respectively (Figure S8).

Subsequently, all atoms in the interface cells were relaxed starting from interface models positioned at their rigid-body equilibrium interface distances, d_0 . These relaxations yield the minimum-energy interface structures. Figure 4 shows the interface models that result from this process. The Cl-terminated interface has a relatively undisturbed interfacial structure, which resembles that of bulk Li and LOC. Li₆O octahedra in LOC at this interface remain intact. On the other hand, large interfacial atomic rearrangements are observed for the O-terminated system. In this case, truncated Li₆O octahedra at the interface (these octahedra are missing a Li atom at the octahedron vertex closest to the Li slab) are reformed by attracting Li atoms from the Li slab. These models were used to calculate thermodynamic properties and the work of adhesion, as described below.

Interface Thermodynamics. We first consider the thermodynamic properties of the LOC/Li interface. These are summarized in Table 2 and include the interface formation energy, the strain energy, and the interface energy. The interface formation energy, G_{f} was calculated as⁶⁸

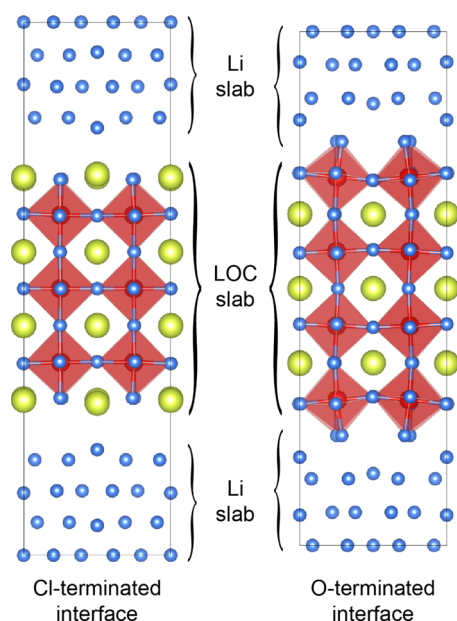


Figure 4. Relaxed structure of Cl- and O-terminated interfaces, which consist of seven layers of LOC (100) and BCC Li (100) planes (103 and 107 atoms, respectively). The O-terminated interface is shorter in height than the Cl-terminated interface due to shorter interlayer distance. A weak interaction is found at the Cl-terminated interface, whereas O ions strongly attract Li-metal atoms and form an octahedron to make up for the missing part at the O-terminated interface.

$$\begin{aligned}
 G_f &= G_{\text{interface}} - n_{\text{Li}}^{\text{Li slab}} G_{\text{Li}}^{\text{BCC bulk}} - \sum_i n_i^{\text{LOC slab}} \mu_i^{\text{LOC}} \\
 &= G_{\text{interface}} - n_{\text{Li}}^{\text{Li slab}} \mu_{\text{Li}}^{\text{ref}} - \left[\frac{1}{3} n_{\text{Li}}^{\text{LOC slab}} G_{\text{Li}_3\text{OCl}}^{\text{bulk}} \right. \\
 &\quad \left. + \left(n_{\text{O}}^{\text{LOC slab}} - \frac{1}{3} n_{\text{Li}}^{\text{LOC slab}} \right) \mu_{\text{O}}^{\text{LOC}} \right. \\
 &\quad \left. + \left(n_{\text{Cl}}^{\text{LOC slab}} - \frac{1}{3} n_{\text{Li}}^{\text{LOC slab}} \right) \mu_{\text{Cl}}^{\text{LOC}} \right] \quad (3)
 \end{aligned}$$

where the allowable range of chemical potentials, $\mu_{\text{O}}^{\text{LOC}}$ and $\mu_{\text{Cl}}^{\text{LOC}}$, is the same as in the surface energy calculations. Here, the second and third terms on the right of the above expression (eq 3) refer to the bulk free energies per atom (Li) or per formula unit (LOC) under zero-strain conditions. Thus, the interface formation energy reflects the energetic cost to form the Li/LOC interface from (unstrained) bulk Li and bulk LOC.

At STP, the calculated formation energies of the Cl- and O-terminated interfaces are 3.80 and 3.21 eV, respectively. (To place these values in context, we note that the formation energies of β'' -Mg₅Si₆/ α -Al interfaces were reported to fall within that range of 0.7–4.5 eV.⁶⁸) These data indicate that

the O termination is energetically favored compared to the Cl termination. The relative ordering of the formation energies is the same under conditions that mimic LOC synthesis (2.84 vs 2.12 eV for Cl and O terminations, respectively; Table 2). Similar to the surface energies, the interfacial formation energies are constant values, i.e., they are independent of the oxygen chemical potential.

The interface formation energy can be expressed as a sum of two terms. These include a strain energy incurred to form a coherent interface (in this case applied only to a Li metal) and the interfacial energy⁶⁸

$$G_f = A\gamma + \zeta$$

Here, γ is the interface energy evaluated for the coherent LOC/Li junction, assuming a strained Li metal. The interface energy is a measure of the interfacial bonding strength. ζ is the strain energy associated with matching the Li in-plane surface lattice constants to that of LOC. The calculated interface energies of Cl- and O-terminated interfaces are 0.50 and 0.42 J/m² at STP and 0.37 and 0.28 J/m² at the LOC synthesis conditions, respectively. As the interface energy is measured relative to the average bonding in LOC and Li metal, the positive values predicted for γ imply that bonding at both interfaces is slightly weaker than on average in the bulk materials. Although the Cl-terminated surface is more stable than the O-terminated variant, the smaller magnitude of the interface energy obtained for the O-terminated interface suggests that the O-terminated interface is preferred relative to the Cl-terminated variant. It is possible that O-terminated interfaces may be formed from the Cl-terminated LOC surface through the segregation of oxygen to the interface. Regarding the strain energy, the computed value is small, only 0.03 eV. This follows from the small size of the strain and the softness of a Li metal. Given that the interface energies of both terminations are comparable, we extend our characterization of their properties to both variants.

Interface Adhesion and Wettability. Using the relaxed interface geometries shown in Figure 4, Table 3 summarizes

Table 3. Calculated Work of Adhesion and Contact Angle as a Function of Interface Composition for the Li/Li₃OCl Interface

interface	work of adhesion (J/m ²)	contact angle (deg)
Cl termination	0.09	143.4
O termination	0.75	52.6

the interfacial work of adhesion, W_{ad} , and the contact angle, θ_{c} , for Li wetting of LOC. A large difference is observed in the W_{ad} values for the two interface terminations. First, adhesion at the Cl-terminated interface is relatively weak, $W_{\text{ad}} = 0.09$ J/m². This weak interaction is consistent with this interface's relatively undistorted atomic structure (Figure 4) and likely

Table 2. Calculated Li/Li₃OCl Interface Formation Energy, Strain Energy, and Interface Energy as a Function of Interface Composition at Ambient Conditions and at Conditions That Mimic the Temperature and Pressure Used during the Synthesis of LOC

interface	300 K at 1 atm			550 K at 10 ⁻⁸ atm		
	formation energy (eV)	strain energy (eV)	interface energy (J/m ²)	formation energy (eV)	strain energy (eV)	interface energy (J/m ²)
Cl termination	3.80	0.03	0.50	2.84	0.03	0.37
O termination	3.21	0.03	0.42	2.12	0.03	0.28

reflects the low reactivity (with Li metal) of the intact Li_6O octahedra present at the interface. In contrast, adhesion at the O-terminated interface is much stronger, $W_{\text{ad}} = 0.75 \text{ J/m}^2$. In this case, the stronger adhesion arises from stronger interactions between the Li-metal slab and the truncated Li_6O octahedra at the LOC surface, Figure 4. Reforming the Li_6O octahedra and extending the LOC crystal structure by scavenging Li from the metal slab provides a driving force for stronger interfacial adhesion.

Prior studies have argued that the wettability of an SE by a Li metal is desirable for achieving low interfacial resistance and for suppressing the formation of dendrites.^{20–22} Wettability is typically evaluated using sessile drop experiments, wherein the contact angle, θ_c , of molten Li on an SE substrate is measured.^{22,69} $\theta_c > 90^\circ$ is associated with weak, nonwetting interfacial interactions, while $\theta_c < 90^\circ$ implies strong interfacial adhesion.⁶⁹ The contact angle can be calculated from W_{ad} and the surface energy of Li, σ_{Li} , via the Young–Dupré equation⁷⁰

$$W_{\text{ad}} = \sigma_{\text{Li}}(1 + \cos \theta_c)$$

Table 3 shows the calculated contact angles for a Li metal on the Cl- and O-terminated surfaces of LOC. Consistent with their relative W_{ad} values, Li is predicted to not wet the Cl-terminated surface, $\theta_c = 143.4^\circ$, but is expected to wet the O-terminated surface, $\theta_c = 52.6^\circ$. The possibility for achieving good Li wettability for the most stable (O-terminated) Li/LOC interface may underlie the good cyclability reported for this system in previous experiments.^{37,38} Nevertheless, since the O-terminated surface of LOC has higher surface energy (compared to the Cl-terminated version, Figure 3), it will be more reactive, for example, toward gas-phase species potentially encountered during its synthesis and handling. New surface compounds formed by these reactions could reduce its wettability by Li, as shown recently for LLZO.²² Thus, realizing the benefits of the O-terminated interface may require additional care in material handling.

Interfacial Electronic Structure and Electrochemical Window. Stability against undesirable electron transfer to or from an SE depends upon the positions of the SE's band edges (CBM and VBM) in relation to the electrochemical potentials of the electrodes. Toward predicting this stability, the spatial distribution of the VBM and CBM of LOC in contact with a Li-metal electrode was identified. Figure 5 shows charge density isosurfaces for the VBM and CBM of the O-terminated LOC/Li interface. These distributions were determined by analyzing the band- and k -point-decomposed partial charge density. Specifically, the VBM was identified as the highest occupied electronic state having the majority of its density located on the LOC slab; similarly, the CBM was identified by searching for the lowest energy unoccupied state with majority weight on the SE. (Additional details describing the process for identifying the band edge states are provided in Figures S9–S12 and in associated descriptions in the Supporting Information.)

Figure 6 illustrates the predicted band edge positions and the corresponding electrochemical window for bulk LOC and for Li/LOC interfaces terminated with Cl or O. Band edge positions for bulk LOC were determined with the aid of a vacuum/slab supercell of LOC; this procedure predicts the behavior of bulk LOC far from surfaces/interfaces and thus does not account for possible changes to the positions of the VBM or CBM due to interfacial interactions near electrodes (in this case, a Li-metal anode). (Bulk band edge positions for

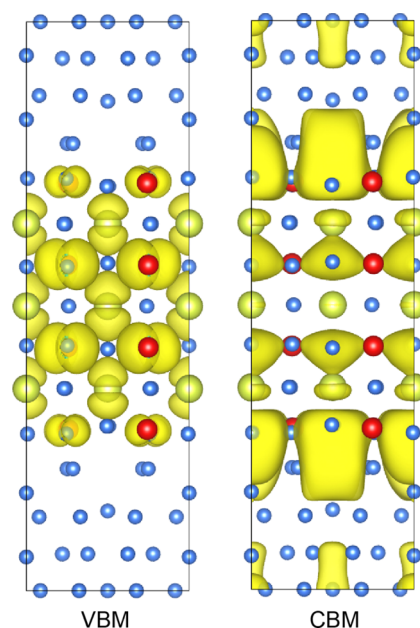


Figure 5. Charge density isosurfaces for the VBM (left) and CBM (right) of the O-terminated Li/LOC interface. Li atoms are blue, oxygen is red, and chlorine is yellow.

a different SE, LLZO, were reported in a prior study.)²⁴ Importantly, the present study also quantifies the extent to which band edge positions change near interfaces (described below). This is done for the two explicit interface models shown in Figure 4.

Assuming a Cl-terminated (100) surface, Figure 6 shows that “isolated” bulk LOC has band edge positions that are well outside of the operating window of a hypothetical Li metal/4.5 V battery. The CBM is located 0.4 eV above the vacuum level and is separated by the bulk band gap (8.04 eV) from the VBM, the latter 7.6 eV below the vacuum level. These band edge positions suggest that, in the limit of isolated/bulk LOC where all interfacial effects are ignored, there is a negligible driving force for electron transfer to/from LOC from either an anode operating at the Li/Li^+ potential or to a cathode operating at 4.5 V.

Assuming the surface of LOC remains Cl-terminated, Figure 6 also shows that interfacing LOC with Li has little effect on the band edge positions. In this case, only minor shifts in the VBM (+0.43 eV) and CBM (+0.04 eV) are predicted; these shifts reduce the band gap slightly, to 7.65 eV. The relatively small shifts introduced by interfacial interactions at the Cl-terminated interface may be explained by the weak interactions present there. As mentioned above, the work of adhesion for this interface is small, only 0.09 J/m^2 . Such weak interactions do not strongly perturb the electronic structure of LOC, leaving the band edge positions relatively unchanged from their positions in the bulk.

Turning to the O-terminated model of LOC, Figure 6 shows that the band edges for the bulk system do not differ significantly from those obtained for the Cl-terminated case: the band edges undergo only a small, 0.3 eV rigid shift to higher energies. Nevertheless, large differences are predicted for the explicit interface model. In contrast to the limited shifts observed for the Cl-terminated interface, the VBM and CBM of LOC at the O-terminated interface shift by +1.29 and -1.15

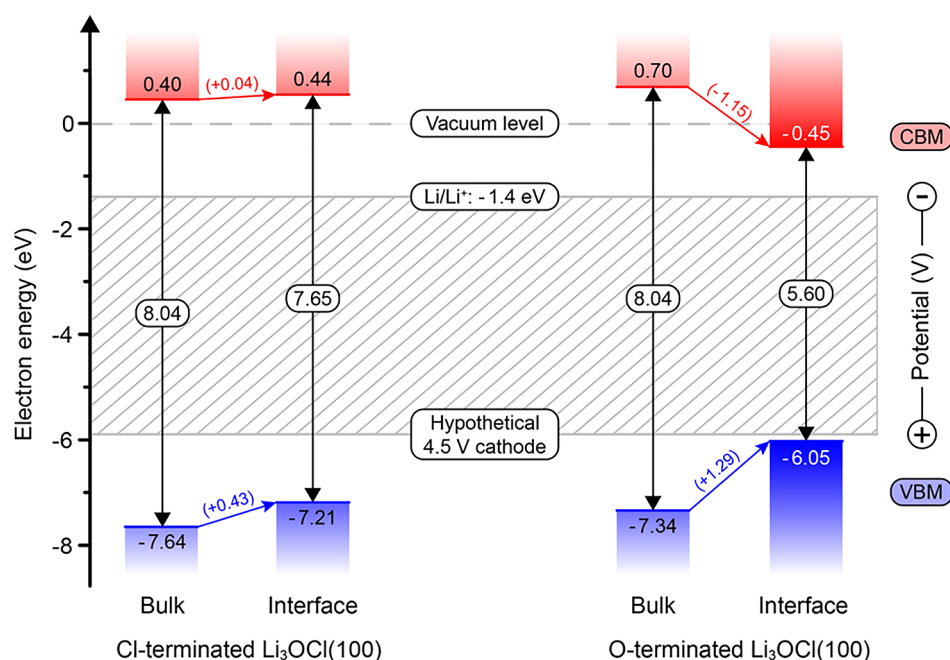


Figure 6. Electrochemical window bulk LOC and for Li/LOC interfaces. Both Cl- and O-terminated interfaces are reported. Red and blue bands indicate the positions of the CBM and VBM, respectively. Numbers in parentheses indicate the amount (in electron volts) by which the band edges shift (with respect to the bulk positions) at an interface with a Li metal. The Li/Li⁺ level and corresponding presumed 4.5 V cathode level are also shown (shaded area). An energy of zero is assigned to the vacuum level, and the Li/Li⁺ level is located 1.4 eV below the vacuum level.⁷³ The electrochemical potential for a hypothetical 4.5 V (relative to Li/Li⁺) cathode is also plotted.

eV, respectively. These shifts narrow the LOC band gap by 2.4 eV, resulting in a smaller near-interface band gap of 5.60 eV.

The relatively larger changes to the CBM and VBM that occur at the O-terminated interface are a consequence of the stronger bonding present there. Recalling the adhesion and contact angle data from Table 3, this interface is predicted to have a work of adhesion that is eight times larger than the Cl-terminated case. Consequently, a Li metal is expected to wet the O-terminated surface of LOC but not the Cl-terminated one. It is likely that these stronger interfacial interactions induce significant perturbations to the LOC interfacial electronic structure (i.e., the formation of new bonds), which, in turn, shift the band edges more substantially.

Despite the strong interactions present at the O-terminated interface, Figure 6 shows that the CBM for this system remains approximately 1 eV higher in energy (~1 V more negative) than the Li/Li⁺ level. This positioning implies that the electron transfer to LOC from a Li-metal electrode is energetically unfavorable for the O-terminated interface (as well as for the Cl-terminated case, as discussed above), a situation that is desirable from the standpoint of electrochemical stability. A previous study of the chemical stability of LOC using the grand potential phase diagram approach concluded that LOC will not decompose into other compounds when in contact with a Li metal.¹⁷ In total, the present and prior calculations suggest that LOC is both chemically and electrochemically stable against a Li metal. This conclusion is in agreement with prior experiments showing that a Li/LOC/Li symmetric cell exhibited stable operation over many cycles, while SEM imaging of the Li/LOC interface found no evidence of new phase formation.³⁷

Regarding oxidative stability, the resistance of LOC to electron-withdrawing reactions depends upon the position of its VBM relative to the electrochemical potential of the

cathode. An initial estimate of this stability can be gleaned from the position of the VBM for isolated/bulk LOC, as shown in Figure 6. In this approximation, LOC appears to be stable for voltages exceeding 5.5 V. However, this stability limit is very likely overestimated; an explicit calculation of the LOC/cathode interface is needed, as done here for the Li/LOC interface, to position the VBM accurately. (In the limit of isolated/bulk LLZO, accounting for changes to the electrochemical potential of Li at the cathode was shown to shift the VBM to higher energies.⁷¹) Regarding chemical reactivity, a previous DFT calculation suggested that LOC will decompose into LiClO₃ and LiCl when in contact with a LiCoO₂ cathode.¹⁷ In contrast, earlier full-cell experiments using the same cathode reported stable operating voltages of up to 4.2 V.³⁷ Nevertheless, capacity fade observed in these experiments for the early stages of cycling could imply the formation of solid electrolyte interphase (SEI) that prevents further reactions and preserves high-voltage operation. Under this scenario, which is commonly observed at the anode of conventional liquid electrolytes, there would be no inconsistency between the calculations and the experiments. Nevertheless, the possibility for SEI formation highlights the need to go beyond stability assessments that are based on thermodynamics alone: kinetic passivation should also be considered.

Examining the data from Tables 2 and 3 and Figure 6 more broadly, it appears that a trade-off exists between the “interfacial compatibility” of LOC with Li and its electrochemical window (as determined by the position of the LOC CBM). Specifically, Tables 2 and 3 show that the O-terminated interface is the most favorable system based on thermodynamics, adhesion, and Li wettability. On the other hand, Figure 6 shows that these favorable interfacial properties come at a cost to expected electrochemical performance; a more

substantial shift of the CBM is observed for the O-terminated interface, resulting in reduced resistance to electron transfer with the negative electrode. Fortunately, for the present LOC-based system, this trade-off appears to be insufficient in magnitude to impact battery performance, as the bulk CBM starts several electron volts above the Li/Li⁺ level, and interfacial effects do not push the CBM below that level. Nevertheless, it is reasonable to speculate that this trend should apply generally, as the formation of relatively stronger (interfacial) bonds generally coincides with larger perturbations to the electronic structure of a bonding couple.⁷² Thus, other SEs whose bulk band edges lie closer to the electrochemical potentials of the electrodes may be more susceptible to electrochemical instability that is induced by strong interfacial bonding. Stated differently, solid electrolytes having excellent wettability by Li may not be optimal choices for minimizing undesirable electron transfer.

It is important to recognize that defects at the interface could influence interfacial properties. However, since neither the identities (interstitials, vacancies, antisite defects, voids, etc.) nor the concentrations of these defects are known, it is not possible to speculate about even the qualitative nature of their impact—for example, do defects increase or decrease adhesion? As a first step in modeling any complex system (such as a realistic interface), it is helpful to have a clear understanding of an appropriate baseline. By examining the defect-free Li/LOC interface, the present study provides such a baseline.

CONCLUSIONS

The present study has probed several properties of a model solid electrolyte/Li-metal interface at the atomic scale. In particular, the interfacial energy, work of adhesion, wettability, band edge shifts, and the electrochemical window were predicted computationally for a system based on the antiperovskite solid electrolyte Li₃OCl (LOC). Vibrational contributions to the enthalpy and entropy were evaluated to estimate surface/interface energies at near-ambient temperatures. Interface wettability was characterized according to the Li contact angle on LOC, derived from the Young–Dupré equation and the calculated interfacial work of adhesion. Stability against reduction by the Li electrode was predicted by determining the positions of the band edges of LOC via GW calculations relative to the Li/Li⁺ level.

These calculations suggest that the oxygen-terminated Li/LOC interface is the most thermodynamically stable. The calculated work of adhesion implies that Li will wet LOC with a low contact angle of ~53°, reflecting strong interfacial bonding and the possibility for low interfacial resistance. On the other hand, this strong interfacial interaction significantly narrows the band gap of LOC in the interfacial region by shifting both the CBM and VBM: in the vicinity of the interface, the size of the bulk band gap, ~8 eV, is reduced to ~5.6 eV, implying a trade-off between strong interfacial bonding/wettability and electrochemical stability. Despite this interface-induced reduction in electrochemical window, the CBM in LOC remains ~1 V more negative than the Li/Li⁺ redox potential, denoting stability against reduction by the anode.

In total, the present study demonstrates how first-principles computational methods can be used to comprehensively characterize interfacial properties that are relevant to the operation of solid-state batteries.

ASSOCIATED CONTENT

Supporting Information

The Supporting Information is available free of charge on the ACS Publications website at DOI: 10.1021/acsami.9b13311.

Supercell of Li₃OCl; cleavage planes and configurations of surfaces; chemical potential correction; Murnaghan equation of state; GW calculation details; Wulff plots; independency of surface energies of (100) planes on $\mu_{\text{O}}^{\text{LOC}}$; surface energy of BCC Li metal; universal binding energy relation (UBER) fitting of adhesive energy; band and *k*-point decomposed partial charge densities; reference electrostatic potential for the slab model; convergence test for band edges of Li₃OCl at interfaces; and error estimate for CBM positions (PDF)

AUTHOR INFORMATION

Corresponding Author

*E-mail: djsiege@umich.edu. Tel: +1 (734) 764-4808.

ORCID

Kwangnam Kim: 0000-0003-1149-1733

Donald J. Siegel: 0000-0001-7913-2513

Notes

The authors declare no competing financial interest.

ACKNOWLEDGMENTS

This work was supported as part of the Joint Center for Energy Storage Research (JCESR), an Energy Innovation Hub funded by the U.S. Department of Energy, Office of Science, Basic Energy Sciences.

REFERENCES

- (1) Goodenough, J. B.; Kim, Y. Challenges for Rechargeable Li Batteries. *Chem. Mater.* **2010**, *22*, 587–603.
- (2) Roth, E. P.; Orendorff, C. J. How Electrolytes Influence Battery Safety. *Electrochem. Soc. Interface* **2012**, *21*, 45–49.
- (3) Goodenough, J. B.; Singh, P. Review—Solid Electrolytes in Rechargeable Electrochemical Cells. *J. Electrochem. Soc.* **2015**, *162*, A2387–A2392.
- (4) Jung, Y. C.; Kim, S. K.; Kim, M. S.; Lee, J. H.; Han, M. S.; Kim, D. H.; Shin, W. C.; Ue, M.; Kim, D. W. Ceramic Separators Based on Li⁺-Conducting Inorganic Electrolyte for High-Performance Lithium-Ion Batteries with Enhanced Safety. *J. Power Sources* **2015**, *293*, 675–683.
- (5) Hu, Y.-S. Batteries: Getting Solid. *Nat. Energy* **2016**, *1*, No. 16042.
- (6) Cho, S.; Kim, S.; Kim, W.; Kim, S.; Ahn, S. All-Solid-State Lithium Battery Working without an Additional Separator in a Polymeric Electrolyte. *Polymers* **2018**, *10*, 1364.
- (7) Monroe, C.; Newman, J. The Impact of Elastic Deformation on Deposition Kinetics at Lithium/Polymer Interfaces. *J. Electrochem. Soc.* **2005**, *152*, A396–A404.
- (8) Albertus, P.; Babinec, S.; Litzelman, S.; Newman, A. Status and Challenges in Enabling the Lithium Metal Electrode for High-Energy and Low-Cost Rechargeable Batteries. *Nat. Energy* **2018**, *3*, 16–21.
- (9) Murugan, R.; Thangadurai, V.; Weppner, W. Fast Lithium Ion Conduction in Garnet-Type Li₇La₃Zr₂O₁₂. *Angew. Chem., Int. Ed.* **2007**, *46*, 7778–7781.
- (10) Deiseroth, H.-J.; Kong, S. T.; Eckert, H.; Vannahme, J.; Reiner, C.; Zaiß, T.; Schlosser, M. Li₆PS₃X: A Class of Crystalline Li-Rich Solids with an Unusually High Li⁺ Mobility. *Angew. Chem., Int. Ed.* **2008**, *47*, 755–758.
- (11) Kamaya, N.; Homma, K.; Yamakawa, Y.; Hirayama, M.; Kanno, R.; Yonemura, M.; Kamiyama, T.; Kato, Y.; Hama, S.; Kawamoto, K.;

Mitsui, A. A Lithium Superionic Conductor. *Nat. Mater.* **2011**, *10*, 682–686.

(12) Zhao, Y.; Daemen, L. L. Superionic Conductivity in Lithium-Rich Anti-Perovskites. *J. Am. Chem. Soc.* **2012**, *134*, 15042–15047.

(13) Richards, W. D.; Tsujimura, T.; Miara, L. J.; Wang, Y.; Kim, J. C.; Ong, S. P.; Uechi, I.; Suzuki, N.; Ceder, G. Design and Synthesis of the Superionic Conductor $\text{Na}_{10}\text{SnP}_2\text{S}_{12}$. *Nat. Commun.* **2016**, *7*, No. 11009.

(14) Kato, Y.; Hori, S.; Saito, T.; Suzuki, K.; Hirayama, M.; Mitsui, A.; Yonemura, M.; Iba, H.; Kanno, R. High-Power All-Solid-State Batteries Using Sulfide Superionic Conductors. *Nat. Energy* **2016**, *1*, No. 16030.

(15) Zhang, Z.; Shao, Y.; Lotsch, B.; Hu, Y.-S.; Li, H.; Janek, J.; Nazar, L. F.; Nan, C.; Maier, J.; Armand, M.; Chen, L. New Horizons for Inorganic Solid State Ion Conductors. *Energy Environ. Sci.* **2018**, *11*, 1945–1976.

(16) Zhu, Y.; He, X.; Mo, Y. First Principles Study on Electrochemical and Chemical Stability of Solid Electrolyte–Electrode Interfaces in All-Solid-State Li-Ion Batteries. *J. Mater. Chem. A* **2016**, *4*, 3253–3266.

(17) Richards, W. D.; Miara, L. J.; Wang, Y.; Kim, J. C.; Ceder, G. Interface Stability in Solid-State Batteries. *Chem. Mater.* **2016**, *28*, 266–273.

(18) Han, F.; Zhu, Y.; He, X.; Mo, Y.; Wang, C. Electrochemical Stability of $\text{Li}_{10}\text{GeP}_2\text{S}_{12}$ and $\text{Li}_7\text{La}_3\text{Zr}_2\text{O}_{12}$ Solid Electrolytes. *Adv. Energy Mater.* **2016**, *6*, No. 1501590.

(19) Rettenwander, D.; Wagner, R.; Reyer, A.; Bonta, M.; Cheng, L.; Doeff, M. M.; Limbeck, A.; Wilkening, M.; Amthauer, G. Interface Instability of Fe-Stabilized $\text{Li}_7\text{La}_3\text{Zr}_2\text{O}_{12}$ versus Li Metal. *J. Phys. Chem. C* **2018**, *122*, 3780–3785.

(20) Han, X.; Gong, Y.; Fu, K. K.; He, X.; Hitz, G. T.; Dai, J.; Pearse, A.; Liu, B.; Wang, H.; Rubloff, G.; Mo, Y.; Thangadurai, V.; Wachsman, E. D.; Hu, L. Negating Interfacial Impedance in Garnet-Based Solid-State Li Metal Batteries. *Nat. Mater.* **2017**, *16*, 572–579.

(21) Li, Y.; Zhou, W.; Chen, X.; Lü, X.; Cui, Z.; Xin, S.; Xue, L.; Jia, Q.; Goodenough, J. B. Mastering the Interface for Advanced All-Solid-State Lithium Rechargeable Batteries. *Proc. Natl. Acad. Sci. U.S.A.* **2016**, *113*, 13313–13317.

(22) Sharafi, A.; Kazyak, E.; Davis, A. L.; Yu, S.; Thompson, T.; Siegel, D. J.; Dasgupta, N. P.; Sakamoto, J. Surface Chemistry Mechanism of Ultra-Low Interfacial Resistance in the Solid-State Electrolyte $\text{Li}_7\text{La}_3\text{Zr}_2\text{O}_{12}$. *Chem. Mater.* **2017**, *29*, 7961–7968.

(23) Kumar, N.; Siegel, D. J. Interface-Induced Renormalization of Electrolyte Energy Levels in Magnesium Batteries. *J. Phys. Chem. Lett.* **2016**, *7*, 874–881.

(24) Thompson, T.; Yu, S.; Williams, L.; Schmidt, R. D.; Garcia-Mendez, R.; Wolfenstine, J.; Allen, J. L.; Kioupakis, E.; Siegel, D. J.; Sakamoto, J. Electrochemical Window of the Li-Ion Solid Electrolyte $\text{Li}_7\text{La}_3\text{Zr}_2\text{O}_{12}$. *ACS Energy Lett.* **2017**, *2*, 462–468.

(25) Ong, S. P.; Mo, Y.; Richards, W. D.; Miara, L.; Lee, H. S.; Ceder, G. Phase Stability, Electrochemical Stability and Ionic Conductivity of the $\text{Li}_{10\pm 1}\text{MP}_2\text{X}_{12}$ (M = Ge, Si, Sn, Al or P, and X = O, S or Se) Family of Superionic Conductors. *Energy Environ. Sci.* **2013**, *6*, 148–156.

(26) Zhang, Y.; Zhao, Y.; Chen, C. Ab Initio Study of the Stabilities of and Mechanism of Superionic Transport in Lithium-Rich Antiperovskites. *Phys. Rev. B: Condens. Matter Mater. Phys.* **2013**, *87*, No. 134303.

(27) Luntz, A. C.; Voss, J.; Reuter, K. Interfacial Challenges in Solid-State Li Ion Batteries. *J. Phys. Chem. Lett.* **2015**, *6*, 4599–4604.

(28) Manthiram, A.; Yu, X.; Wang, S. Lithium Battery Chemistries Enabled by Solid-State Electrolytes. *Nat. Rev. Mater.* **2017**, *2*, No. 16103.

(29) Luo, W.; Gong, Y.; Zhu, Y.; Li, Y.; Yao, Y.; Zhang, Y.; Fu, K. K.; Pastel, G.; Lin, C. F.; Mo, Y.; Wachsman, E. D.; Hu, L. Reducing Interfacial Resistance between Garnet-Structured Solid-State Electrolyte and Li-Metal Anode by a Germanium Layer. *Adv. Mater.* **2017**, *29*, No. 1606042.

(30) Tsai, C.-L.; Roddatis, V.; Chandran, C. V.; Ma, Q.; Uhlenbruck, S.; Bram, M.; Heitjans, P.; Guillon, O. $\text{Li}_7\text{La}_3\text{Zr}_2\text{O}_{12}$ Interface Modification for Li Dendrite Prevention. *ACS Appl. Mater. Interfaces* **2016**, *8*, 10617–10626.

(31) Braga, M. H.; Grundish, N. S.; Murchison, A. J.; Goodenough, J. B. Alternative Strategy for a Safe Rechargeable Battery. *Energy Environ. Sci.* **2017**, *10*, 331–336.

(32) Wang, C.; Gong, Y.; Liu, B.; Fu, K.; Yao, Y.; Hitz, E.; Li, Y.; Dai, J.; Xu, S.; Luo, W.; Wachsman, E. D.; Hu, L. Conformal, Nanoscale ZnO Surface Modification of Garnet-Based Solid-State Electrolyte for Lithium Metal Anodes. *Nano Lett.* **2017**, *17*, 565–571.

(33) Fu, K. K.; Gong, Y.; Liu, B.; Zhu, Y.; Xu, S.; Yao, Y.; Luo, W.; Wang, C.; Lacey, S. D.; Dai, J.; Chen, Y.; Mo, Y.; Wachsman, E.; Hu, L. Toward Garnet Electrolyte-Based Li Metal Batteries: An Ultrathin, Highly Effective, Artificial Solid-State Electrolyte/Metallic Li Interface. *Sci. Adv.* **2017**, *3*, No. e1601659.

(34) Wang, Y.; Wang, Q.; Liu, Z.; Zhou, Z.; Li, S.; Zhu, J.; Zou, R.; Wang, Y.; Lin, J.; Zhao, Y. Structural Manipulation Approaches towards Enhanced Sodium Ionic Conductivity in Na-Rich Antiperovskites. *J. Power Sources* **2015**, *293*, 735–740.

(35) Kim, K.; Siegel, D. J. Correlating Lattice Distortions, Ion Migration Barriers, and Stability in Solid Electrolytes. *J. Mater. Chem. A* **2019**, *7*, 3216–3227.

(36) Emly, A.; Kioupakis, E.; Van der Ven, A. Phase Stability and Transport Mechanisms in Antiperovskite Li_3OCl and Li_3OB Superionic Conductors. *Chem. Mater.* **2013**, *25*, 4663–4670.

(37) Lü, X.; Howard, J. W.; Chen, A.; Zhu, J.; Li, S.; Wu, G.; Dowden, P.; Xu, H.; Zhao, Y.; Jia, Q. Antiperovskite Li_3OCl Superionic Conductor Films for Solid-State Li-Ion Batteries. *Adv. Sci.* **2016**, *3*, No. 1500359.

(38) Lü, X.; Wu, G.; Howard, J. W.; Chen, A.; Zhao, Y.; Daemen, L. L.; Jia, Q. Li-Rich Anti-Perovskite Li_3OCl Films with Enhanced Ionic Conductivity. *Chem. Commun.* **2014**, *50*, 11520–11522.

(39) Kresse, G.; Furthmüller, J. Efficient Iterative Schemes for Ab Initio Total-Energy Calculations Using a Plane-Wave Basis Set. *Phys. Rev. B: Condens. Matter Mater. Phys.* **1996**, *54*, 11169–11186.

(40) Perdew, J. P.; Burke, K.; Ernzerhof, M. Generalized Gradient Approximation Made Simple. *Phys. Rev. Lett.* **1996**, *77*, 3865–3868.

(41) Blöchl, P. E. Projector Augmented-Wave Method. *Phys. Rev. B: Condens. Matter Mater. Phys.* **1994**, *50*, 17953–17979.

(42) Kresse, G.; Joubert, D. From Ultrasoft Pseudopotentials to the Projector Augmented-Wave Method. *Phys. Rev. B: Condens. Matter Mater. Phys.* **1999**, *59*, 1758–1775.

(43) Wei, S.; Chou, M. Y. Ab Initio Calculation of Force Constants and Full Phonon Dispersions. *Phys. Rev. Lett.* **1992**, *69*, 2799–2802.

(44) Aryasetiawan, F.; Gunnarsson, O. The GW Method. *Rep. Prog. Phys.* **1998**, *61*, 237–312.

(45) Shishkin, M.; Kresse, G. Implementation and Performance of the Frequency-Dependent GW Method within the PAW Framework. *Phys. Rev. B: Condens. Matter Mater. Phys.* **2006**, *74*, No. 035101.

(46) Shishkin, M.; Kresse, G. Self-Consistent GW Calculations for Semiconductors and Insulators. *Phys. Rev. B: Condens. Matter Mater. Phys.* **2007**, *75*, No. 235102.

(47) Fuchs, F.; Furthmüller, J.; Bechstedt, F.; Shishkin, M.; Kresse, G. Quasiparticle Band Structure Based on a Generalized Kohn-Sham Scheme. *Phys. Rev. B: Condens. Matter Mater. Phys.* **2007**, *76*, No. 115109.

(48) Toroker, M. C.; Kanan, D. K.; Alidoust, N.; Isseroff, L. Y.; Liao, P.; Carter, E. A. First Principles Scheme to Evaluate Band Edge Positions in Potential Transition Metal Oxide Photocatalysts and Photoelectrodes. *Phys. Chem. Chem. Phys.* **2011**, *13*, 16644.

(49) Grüneis, A.; Kresse, G.; Hinuma, Y.; Oba, F. Ionization Potentials of Solids: The Importance of Vertex Corrections. *Phys. Rev. Lett.* **2014**, *112*, No. 096401.

(50) Hinuma, Y.; Grüneis, A.; Kresse, G.; Oba, F. Band Alignment of Semiconductors from Density-Functional Theory and Many-Body Perturbation Theory. *Phys. Rev. B* **2014**, *90*, No. 155405.

(51) Heyd, J.; Scuseria, G. E.; Ernzerhof, M. Hybrid Functionals Based on a Screened Coulomb Potential. *J. Chem. Phys.* **2003**, *118*, 8207–8215.

(52) Krukau, A. V.; Vydrov, O. A.; Izmaylov, A. F.; Scuseria, G. E. Influence of the Exchange Screening Parameter on the Performance of Screened Hybrid Functionals. *J. Chem. Phys.* **2006**, *125*, No. 224106.

(53) Hinuma, Y.; Oba, F.; Kumagai, Y.; Tanaka, I. Ionization Potentials of (112) and (112-) Facet Surfaces of CuInSe₂ and CuGaSe₂. *Phys. Rev. B: Condens. Matter Mater. Phys.* **2012**, *86*, No. 245433.

(54) Wallace, D. C. *Thermodynamics of Crystals*; John Wiley & Sons: New York, 1972.

(55) Siegel, D. J.; Wolverton, C.; Ozolidņš, V. Reaction Energetics and Crystal Structure of Li₄BN₃H₁₀ from First Principles. *Phys. Rev. B: Condens. Matter Mater. Phys.* **2007**, *75*, No. 014101.

(56) Rogal, J. *Stability, Composition and Function of Palladium Surfaces in Oxidizing Environments: A First-Principles Statistical Mechanics Approach*; Freie Universität Berlin, 2006.

(57) Ong, S. P.; Wang, L.; Kang, B.; Ceder, G. Li–Fe–P–O₂ Phase Diagram from First Principles Calculations. *Chem. Mater.* **2008**, *20*, 1798–1807.

(58) Chase, M. W. *NIST-JANAF Thermochemical Tables*, 4th ed.; American Institute of Physics: Melville, NY, 1998.

(59) Murnaghan, F. D. The Compressibility of Media under Extreme Pressures. *Proc. Natl. Acad. Sci. U.S.A.* **1944**, *30*, 244–247.

(60) Shishkin, M.; Marsman, M.; Kresse, G. Accurate Quasiparticle Spectra from Self-Consistent GW Calculations with Vertex Corrections. *Phys. Rev. Lett.* **2007**, *99*, No. 246403.

(61) Chen, H. M.; Maohua, C.; Adams, S. Stability and Ionic Mobility in Argyrodite-Related Lithium-Ion Solid Electrolytes. *Phys. Chem. Chem. Phys.* **2015**, *17*, 16494–16506.

(62) Zhu, H.; Aindow, M.; Ramprasad, R. Stability and Work Function of TiC_xN_{1-x} Alloy Surfaces: Density Functional Theory Calculations. *Phys. Rev. B: Condens. Matter Mater. Phys.* **2009**, *80*, No. 201406(R).

(63) Zucker, R. V.; Chatain, D.; Dahmen, U.; Hagege, S.; Carter, W. C. New Software Tools for the Calculation and Display of Isolated and Attached Interfacial-Energy Minimizing Particle Shapes. *J. Mater. Sci.* **2012**, *47*, 8290–8302.

(64) Smith, J. R.; Hong, T.; Srolovitz, D. J. Metal-Ceramic Adhesion and the Harris Functional. *Phys. Rev. Lett.* **1994**, *72*, 4021–4024.

(65) Seriani, N. Ab Initio Thermodynamics of Lithium Oxides: From Bulk Phases to Nanoparticles. *Nanotechnology* **2009**, *20*, No. 445703.

(66) Jäckle, M.; Groß, A. Microscopic Properties of Lithium, Sodium, and Magnesium Battery Anode Materials Related to Possible Dendrite Growth. *J. Chem. Phys.* **2014**, *141*, No. 174710.

(67) Liu, Z.; Qi, Y.; Lin, Y. X.; Chen, L.; Lu, P.; Chen, L. Q. Interfacial Study on Solid Electrolyte Interphase at Li Metal Anode: Implication for Li Dendrite Growth. *J. Electrochem. Soc.* **2016**, *163*, A592–A598.

(68) Wang, Y.; Liu, Z. K.; Chen, L. Q.; Wolverton, C. First-Principles Calculations of B''-Mg₅Si₆/α-Al Interfaces. *Acta Mater.* **2007**, *55*, 5934–5947.

(69) Yuan, Y.; Lee, T. R. Surface Science Techniques. In *Surface Science Techniques*; Bracco, G., Holst, B., Eds.; Springer Series in Surface Sciences; Springer: Heidelberg, 2013; Vol. 51, pp 3–34.

(70) Young, T. An Essay on the Cohesion of Fluids. *Philos. Trans. R. Soc. London* **1805**, *95*, 65–87.

(71) Yu, S. *Atomic Scale Simulations of the Solid Electrolyte Li-La₃Zr₂O₁₂*; University of Michigan: Ann Arbor, MI, 2018.

(72) Hoffmann, R. *Solids and Surfaces: A Chemist's View of Bonding in Extended Structures*; VCH Publishers: New York, NY, 1988.

(73) Borodin, O.; Behl, W.; Jow, T. R. Oxidative Stability and Initial Decomposition Reactions of Carbonate, Sulfone, and Alkyl Phosphate-Based Electrolytes. *J. Phys. Chem. C* **2013**, *117*, 8661–8682.